Supplementary Information

Boosting Z-scheme water splitting via increasing electron transport by manipulating multiple redox-active sites and potentials in metal hexacyanoferrate modifiers

Harutaka Ninomiya,[a] Osamu Tomita,[a] Hajime Suzuki,[a,b] Akinobu Nakada,[a] Rie Haruki,[c] Shunsuke Nozawa,[c] and Ryu Abe*[a]

[a] *Department of Energy and Hydrocarbon Chemistry, Graduate School of Engineering, Kyoto University, Nishikyo-ku, Kyoto 615-8510, Japan. *E-mail: ryu-abe@scl.kyoto-u.ac.jp*

[b] *Precursory Research for Embryonic Science and Technology (PRESTO), Japan Science and Technology Agency (JST), Kawaguchi, Saitama 332-0012, Japan*

[c] *Photon Factory (PF), Institute of Materials Structure Science (IMSS), High Energy Accelerator Research Organization (KEK), Tsukuba, Ibaraki 305-0801, Japan*

Experimental

Reagents

All aqueous solutions were prepared with Milli-Q ultrapure water (18.2 MΩ·cm at 25 °C). The manufacturers and purity of the reagents were as follows: $InCl_3 \cdot 4H_2O$ (Kanto Chemical Co., Inc., 99.95%), $MnCl_2 \cdot 4H_2O$ (FUJIFILM Wako Pure Chemical Co., Inc., 99.0%), $FeCl_2 \cdot 4H_2O$ (FUJIFILM Wako Pure Chemical Co., Inc., 99.0–102.2%), $CoCl_2 \cdot 6H_2O$ (FUJIFILM Wako Pure Chemical Co., Inc., 99.5%), $NiCl_2 \cdot 6H_2O$ (FUJIFILM Wako Pure Chemical Co., Inc., 98.0%), $CuCl_2 \cdot 4H_2O$ (FUJIFILM Wako Pure Chemical Co., Inc., 99.9%), $K_4[Fe(CN)_6] \cdot 3H_2O$ (Kishida Chemical Co., Ltd., 99.5%), $K_3[Fe(CN)_6]$ (FUJIFILM Wako Pure Chemical Co., Inc., 99%), $ZrO(NO_3)_2 \cdot 2H_2O$ (Kanto Chemical Co., Inc., 99.0%), Ta_2O_5 (Kojundo Chemical Co., Ltd., 99.9%), $Na_3RhCl_6 \cdot nH_2O$ (Kanto Chemical Co., Inc., >80.0%), K_2CrO_4 (FUJIFILM Wako Pure Chemical Co., Inc., 99.0%), Bi_2O_3 (FUJIFILM Wako Pure Chemical Co., Inc., 98%), BiOCl (FUJIFILM Wako Pure Chemical Co., Inc., 95.0%), NaCl (FUJIFILM Wako Pure Chemical Co., Inc., 99.5%), CsCl (FUJIFILM Wako Pure Chemical Co., Inc., 99.0%), $FeCl_3 \cdot 6H_2O$ (FUJIFILM Wako Pure Chemical Co., Inc., 99.5%), $RuCl_3 \cdot nH_2O$ (FUJIFILM Wako Pure Chemical Co., Inc., 36–44% as Ru metal), $Na_2SiO_3 \cdot 9H_2O$ (FUJIFILM Wako Pure Chemical Co., Inc., 98.0%), $Na_2WO_4 \cdot 2H_2O$ (FUJIFILM Wako Pure Chemical Corporation, 99.0–100.5%), $VOSO_4 \cdot nH_2O$ (FUJIFILM Wako Pure Chemical Corporation, 99.9%), HCl (FUJIFILM Wako Pure Chemical Corporation, 35.0–37.0%), KCl (FUJIFILM Wako Pure Chemical Co., Inc., 99.5%), H_3BO_3 (FUJIFILM Wako Pure Chemical Co., Inc., 99.5%), CH_3COOH (FUJIFILM Wako Pure Chemical Co., Inc.), CH_3COONa (Kanto Chemical Co., Inc., >99.0%), KH_2PO_4 (FUJIFILM Wako Pure Chemical Corporation, 99.5%).

Characterization of synthesized samples

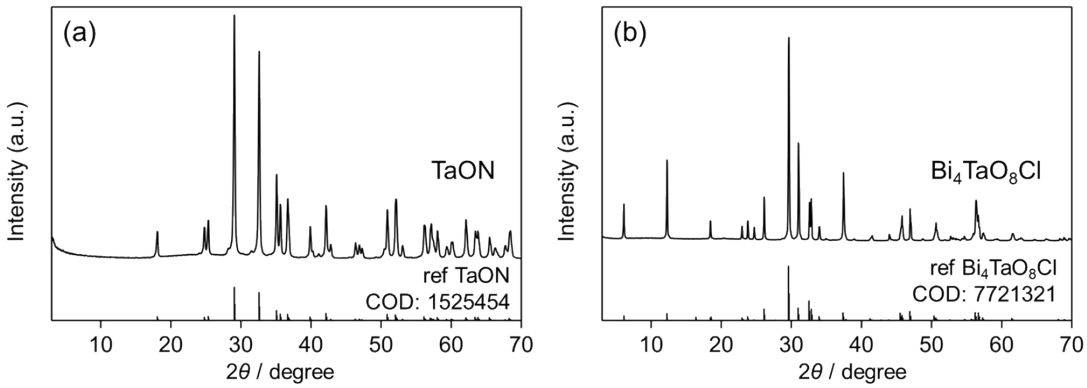

Figure S1. XRD patterns of synthesized samples: (a) TaON and (b) Bi_4TaO_8Cl. Reference patterns obtained from the Crystallography Open Database (COD 1525454 for TaON and COD 7221321 for Bi_4TaO_8Cl) are shown for comparison.[1,2]

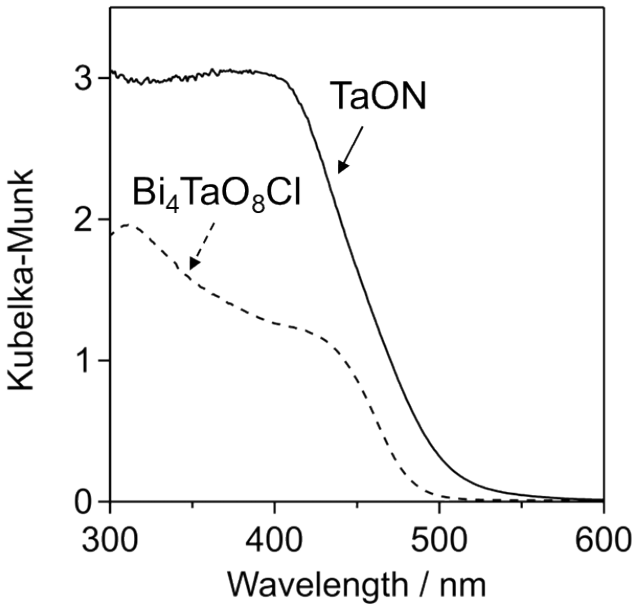

Figure S2. UV–Vis diffuse reflectance spectra of TaON and Bi_4TaO_8Cl.

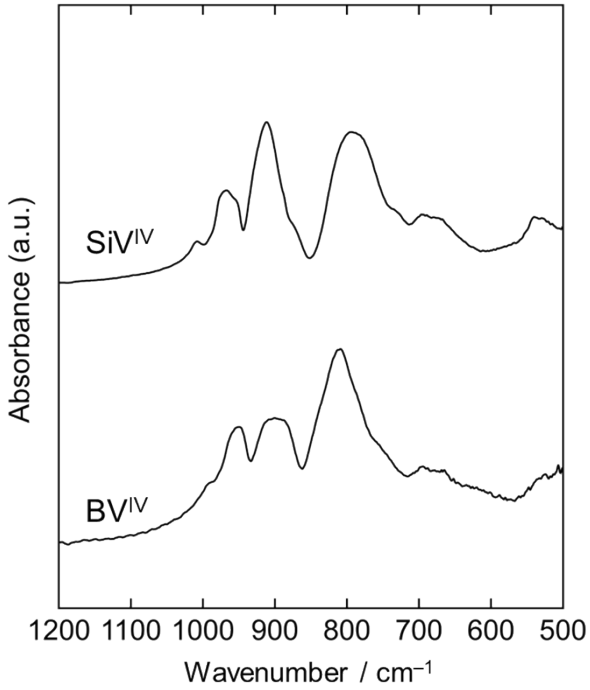

Figure S3. FT-IR spectra of polyoxometalate: SiV^{IV} ($K_6[\alpha\text{-}SiV^{IV}W_{11}O_{40}]\cdot 11H_2O$) and BV^{IV} ($K_7[\alpha\text{-}BV^{IV}W_{11}O_{40}]\cdot 7H_2O$). For the measurements, the samples were ground and diluted to 1 wt% with KBr, followed by pelletization. The spectral pattern and the peak wavenumbers are in good agreement with those reported previously.[3–5]

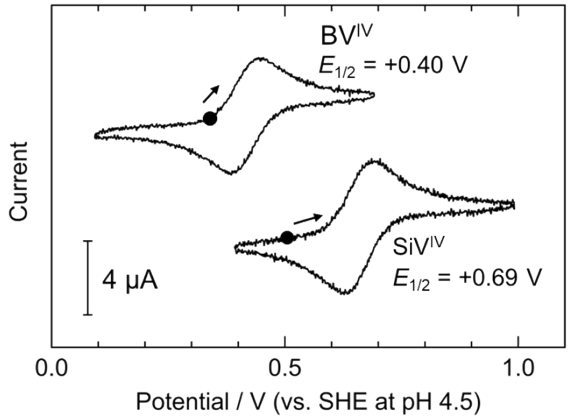

Figure S4. CVs of 0.5 mM SiV^{IV} and BV^{IV} in an aqueous solution of 0.05 M KH_2PO_4 (pH 4.5). A glassy carbon electrode was used as the working electrode, Pt as the counter electrode, and Ag/AgCl as the reference electrode. The scan rate was 50 mV s^{-1}. Black circles denote the open circuit potential for each POM solution.

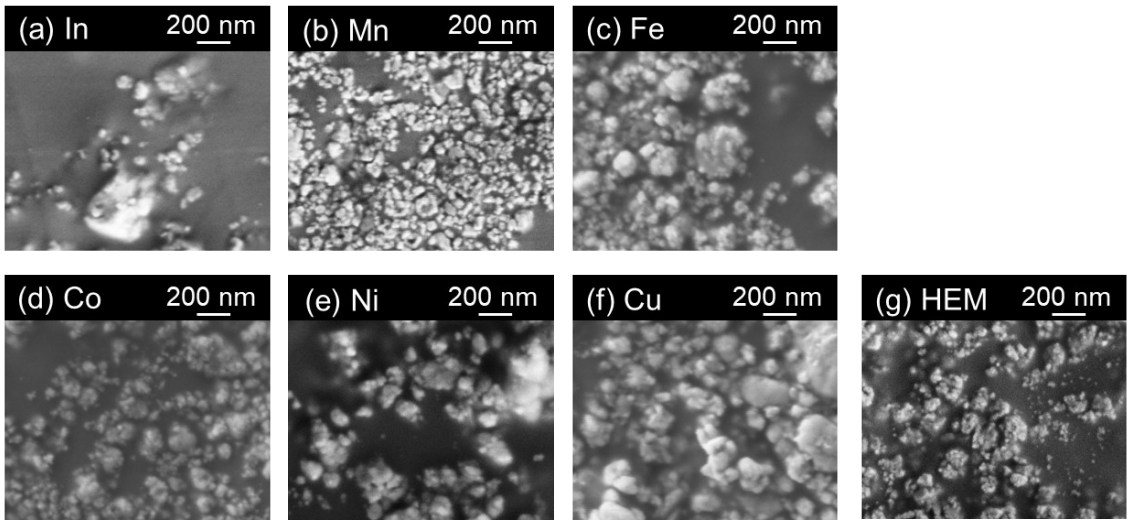

Figure S5. SEM images of MHCFs with $Fe_C = Fe^{II}$. Note that the dark, smooth background is carbon tape.

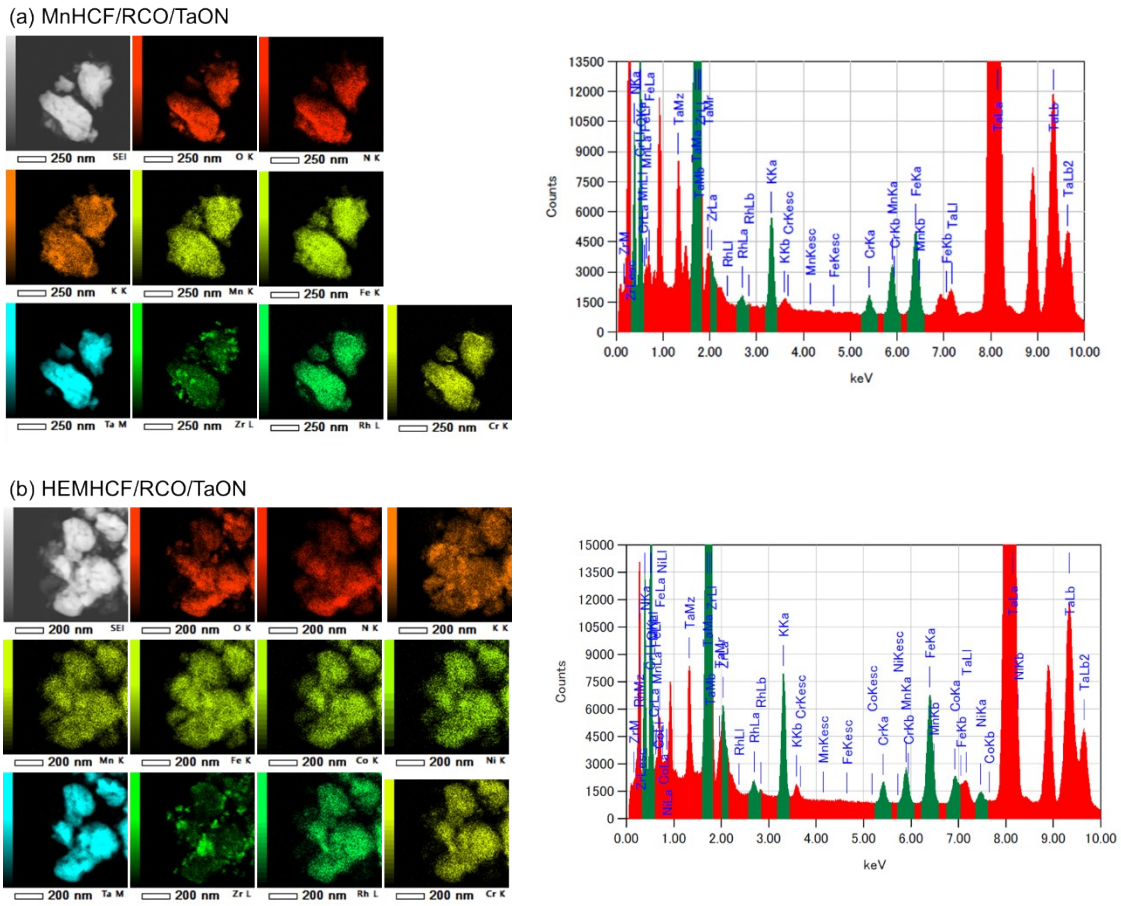

Figure S6. STEM-EDS elemental mappings and spectra of (a) MnHCF/RCO/TaON and (b) HEMHCF. EDS signals of the metal species constituting MHCFs (Mn, Fe, Co, and Ni) were observed on and around the Ta-mapped regions, suggesting that the MHCFs covered the TaON surface as layers with a thickness of several tens of nanometers.

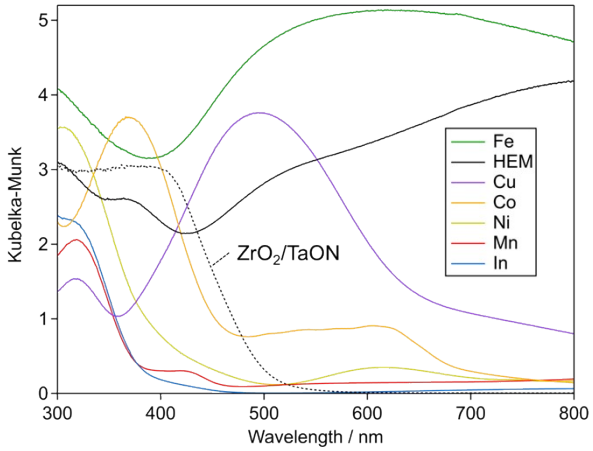

Figure S7. UV–Vis diffuse reflectance spectra of MHCFs with $Fe_C = Fe^{II}$, along with that of TaON.

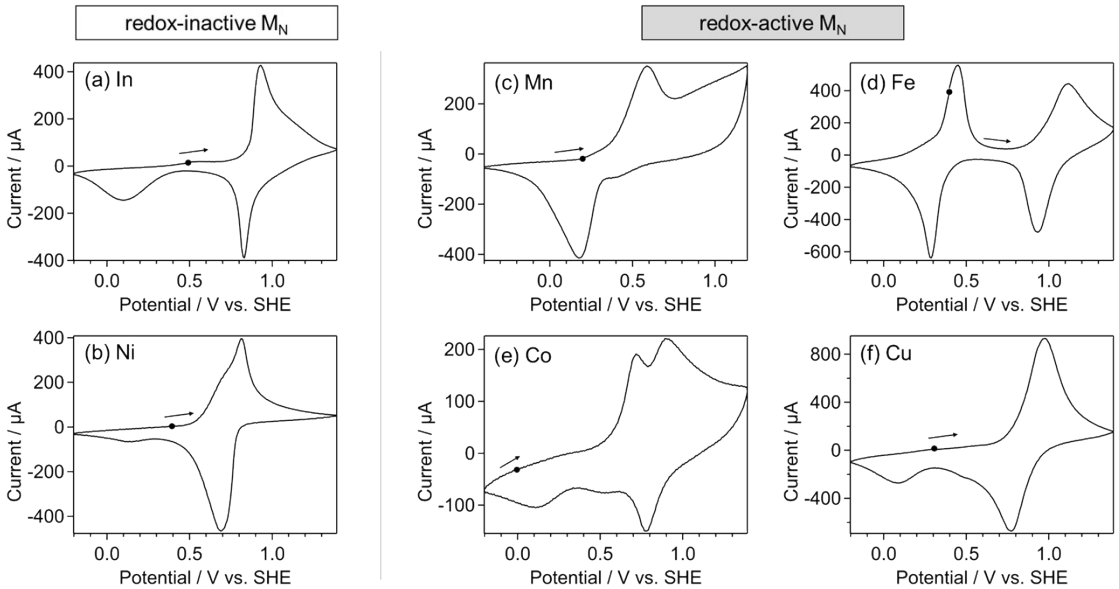

Figure S8. CVs of MHCFs with redox-inactive M_N ((a) InHCF, (b) NiHCF) and redox-active M_N ((c) MnHCF, (d) FeHCF, (e) CoHCF, and (f) CuHCF) in 0.05 M KH_2PO_4 aqueous solution. Initial potential was set to the open rest potential, and scanning began in the anodic direction (50 mV s^{-1}).

CVs of redox-active MHCFs and redox-inactive MHCFs with single M_N species measured in an aqueous medium are provided in **Figure S8**. The irreversible reduction peak at approximately +0.1 V to a greater or lesser extent likely arise from the reduction of dissolved $[Fe^{III}(CN)_6]^{3-}$, which is supported by the fact that these cathodic currents are exhibited only after the anodic scan and oxidizing Fe_C^{II} to Fe_C^{III}; further, a previous report indicates that some of the oxidized MHCFs with Fe_C^{III} are partially soluble in water depending on the M_N species.[6] The assignments of the redox peaks in the CVs of each MHCF are described below.

InHCF and NiHCF display a pair of redox peaks with half-wave potential ($E_{1/2}$) at +0.87 V and +0.75 V vs SHE, respectively, assignable to $Fe_C^{III/II}$.[7,8]

Although CuHCF appears to have a single redox couple in the wide scan CV (**Figure S8(f)**), previous reports state that the $Cu^{II/I}$ in CuHCF is redox-active, exhibiting another, smaller but detectable, pair of redox peaks with an $E_{1/2}$ of ~+0.16 V vs SHE.[9–11] Two distinct $Cu^{II/I}$ redox sites have been proposed: one associated with Cu species located at interstitial sites and the other with Cu species incorporated in the lattice, coordinated to the nitrogen atoms of the cyanide ligands.[9,11,12] As shown in **Figure S9**, the CV measured over a narrowed potential window (0–0.65 V vs SHE) exhibits two oxidation peaks at +0.54 and +0.33 V (A and B), along with a broad reduction peak centered at approximately +0.16 V (C). These features are not discernible in the wide-scan CVs (**Figure S8(f)**). Notably, the oxidation peak A was not observed at the 1st anodic scan (curves with black color), which started at approximately +0.5 V (i.e., each rest potential), but appeared at the 2nd anodic scan after the cathodic scan beyond +0.3 V, at which the cathodic peak C appeared to rise. Because CuHCF was synthesized using a Cu^{II} precursor, the Cu species

in the as-prepared material were expected to be in the divalent state. Therefore, the appearance of peak A only after the first cathodic scan could be attributed to the oxidation of Cu^{I} to Cu^{II}, formed during the first cathodic scan. The intensity of oxidation peak A increased as the cathodic-to-anodic turning potential became more negative, from +0.3 to 0 V, while peak B increased markedly below +0.2 V, indicating that both A and B were coupled to the reduction peak C, which appeared broad owing to the close potentials of the two reduction processes. Peak A was assigned to the oxidation of interstitial Cu species, while peak B arose from lattice Cu species coordinated to cyanide nitrogen. Accordingly, the following discussion focuses on the two redox-active species in CuHCF: lattice $Cu^{II/I}$ and $Fe_C^{III/II}$ ($E_{1/2}$ = +0.24 V and +0.88 V).

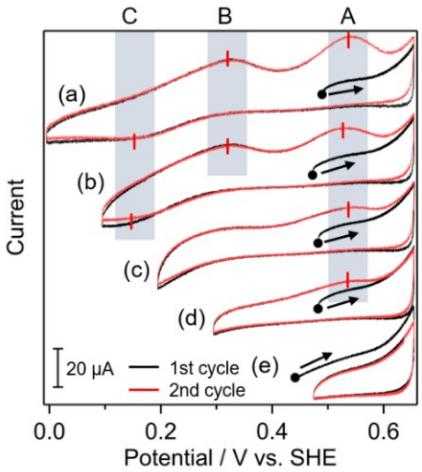

Figure S9. CVs of CuHCF in 0.05 M KH_2PO_4 aqueous solution (pH 4.5) with sequentially expanded scan windows: (a) 0.0–0.65 V, (b) 0.10–0.65 V, (c) 0.20–0.65 V, (d) 0.29–0.65 V, and (e) 0.45–0.65 V vs SHE. Scans started from the rest potential in the cathodic direction.

FeHCF (Prussian blue) and CoHCF exhibited two distinct redox couples (**Figure S8(d),(e)**). In FeHCF, the positive and negative peaks corresponded to $Fe^{III/II}$ coordinated to carbon ($Fe_C^{III/II}$: +1.03 V) and nitrogen ($Fe_N^{III/II}$: +0.37 V), respectively, whereas in CoHCF, they corresponded to $Co^{III/II}$ (+0.84 V) and $Fe_C^{III/II}$ (+0.62 V).[13,14]

Although previous reports revealed that Mn in MnHCF was redox-active and exhibited two distinct redox couples assigned to $Mn^{III/II}$ and $Fe_C^{III/II}$ in organic solution,[13,15] the CV of MnHCF measured in aqueous media (**Figure S8(c)**) did not display two distinct redox couples. Instead, its voltammetric profile more closely resembled those of MnO_2 and $MnCl_2$ in water (**Figure S10(a)**) than that of MnHCF in acetonitrile (**Figure S10(b),(c)**). This is likely due to disproportionation of the Mn^{III} species released during the anodic scan: $2Mn^{III} + 2H_2O \rightarrow Mn^{II} + MnO_2 + 4H^+$.[16–19] Therefore, the decomposition of MnHCF via Mn^{III} species, together with the dissolution of $[Fe^{III}(CN)_6]^{3-}$ and/or $[Fe^{II}(CN)_6]^{4-}$, produces Mn^{II} species and MnO_2 that account for the dominant currents. Indeed, the CV of MnHCF in acetonitrile solution exhibited two distinct pairs of redox waves (**Figure S10(b),(c)**), unlike MnO_2, with similar $E_{1/2}$ to those reported previously.[15] These experiments imply that MnHCF has intrinsic instability when used in aqueous media.

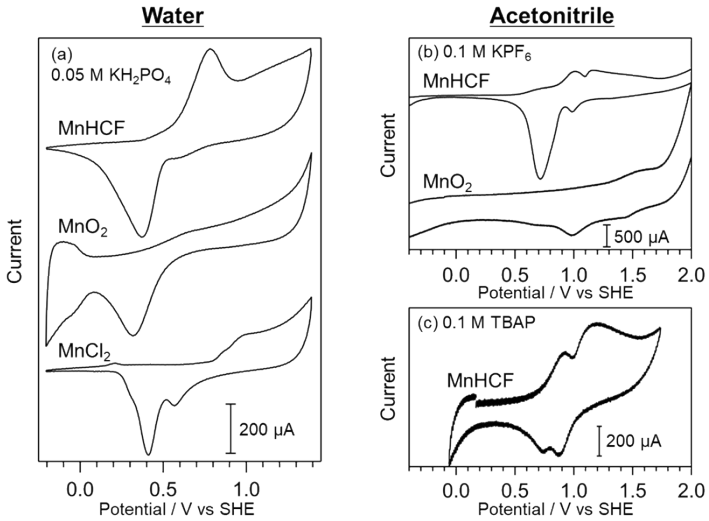

Figure S10. CVs of MnHCF, MnO_2, and $MnCl_2$ in (a) an aqueous solution of 0.05 M KH_2PO_4 (pH 4.5), and an acetonitrile solution of (b) 0.1 M KPF_6 and (c) 0.1 M tetrabutylammonium perchloride (TBAP).

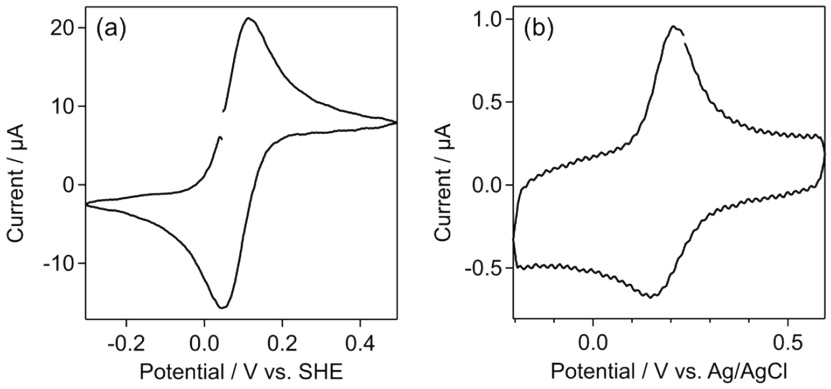

Figure S11. CVs of ferrocene (Fc) in (a) 0.1 M KPF_6 acetonitrile solution and (b) 0.05 M KH_2PO_4 aqueous solution. The half-wave potential of Fc^+/Fc was estimated as +0.079 V vs. Ag/Ag^+ (0.01 M $AgNO_3$, 0.1 M tetrabutylammonium perchloride acetonitrile solution) and +0.188 V vs. Ag/AgCl (3 M NaCl aqueous solution). Given that the standard potential of Ag/AgCl (3 M NaCl aqueous, 25 °C) is +0.195 V vs. SHE, the potential can be converted using the following equation:

E(V vs SHE) = E(V vs Ag/Ag^+) + 0.304.

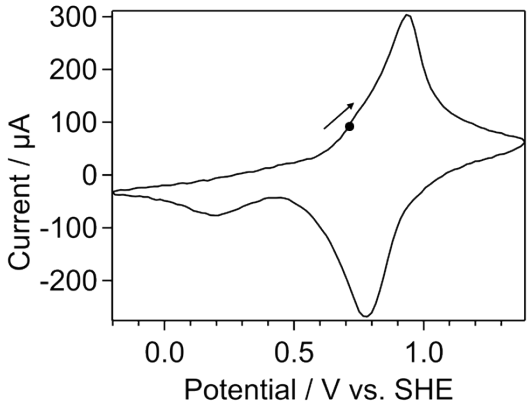

Figure S12. CVs of HEMHCF in 0.05 M KH_2PO_4 aqueous solution. Initial potential was set to the open rest potential, and scanning began in the anodic direction (50 mV s^{-1}).

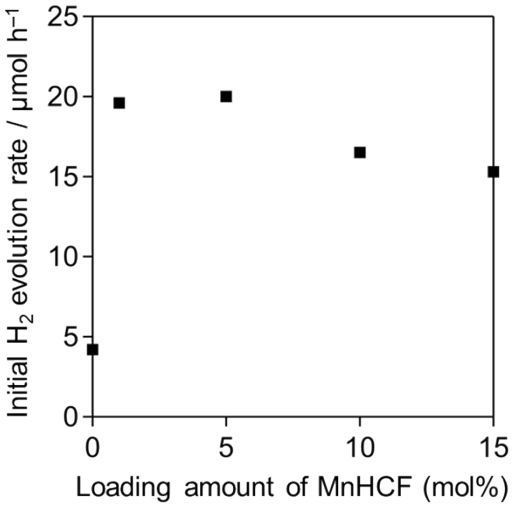

Figure S13. Dependence of the initial H_2 evolution rate on the MnHCF loading amount. Photocatalytic reactions were conducted using 25 mg of RCO/TaON modified with different MnHCF loading amounts in 0.05 M aqueous KH_2PO_4 containing 1 mM SiV^{IV} under visible-light irradiation ($\lambda > 400$ nm).

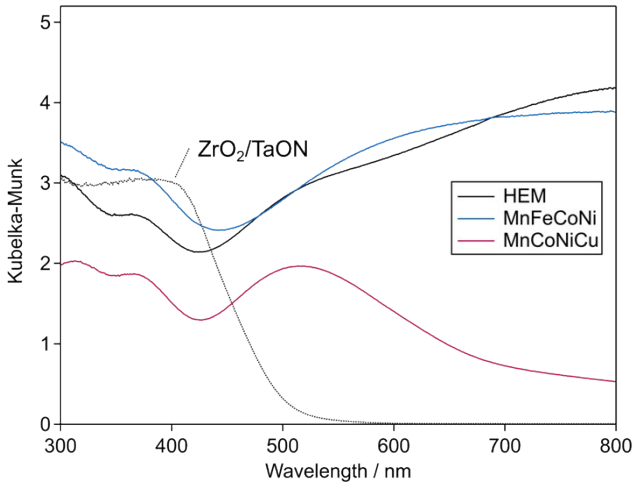

Figure S14. UV–Vis diffuse reflectance spectra of MHCFs (M_N = HEM, MnFeCoNi, MnCoNiCu) with $Fe_C = Fe^{II}$ overlaying that of ZrO_2/TaON.

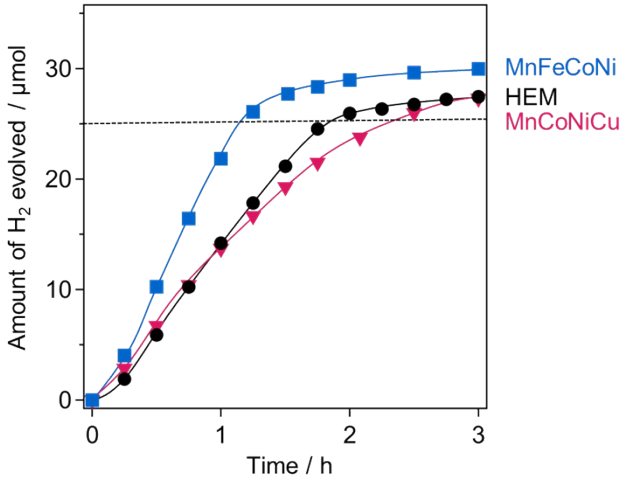

Figure S15. Time course of H_2 evolution under visible light irradiation over MHCF (M = HEM, MnFeCoNi, and MnCoNiCu) modified RCO/TaON in the presence of 0.5 mM SiV^{IV} in aqueous KH_2PO_4 solution (50 mM KH_2PO_4, pH 4.5, 100 mL). Dotted lines show the amount of H_2 evolution corresponding to one electron donation by SiV^{IV}.

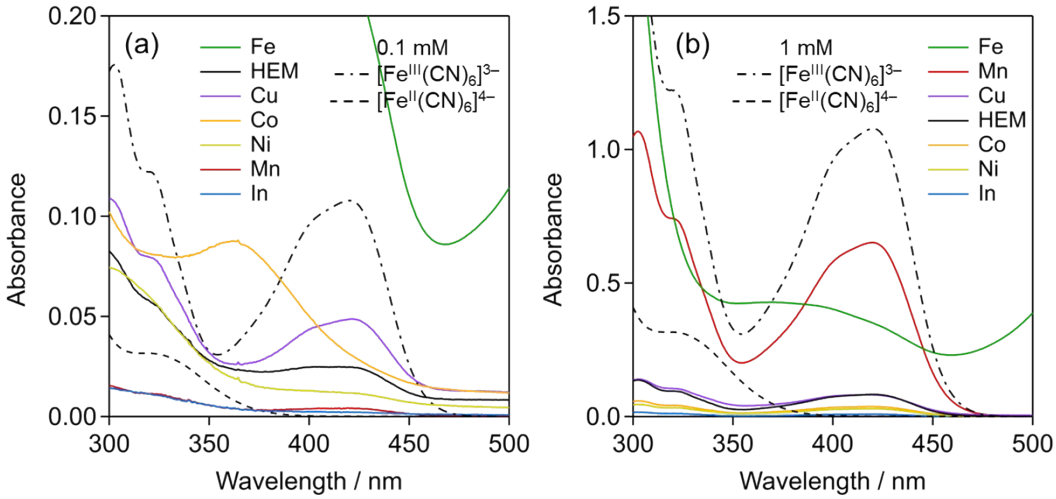

Figure S16. UV–Vis absorption spectra of the solution filtered after stirring MHCF particles in pure water with a magnetic stirrer: (a) $Fe_C = Fe^{II}$ and (b) $Fe_C = Fe^{III}$, along with those of $[Fe^{III}(CN)_6]^{3-}$ and $[Fe^{II}(CN)_6]^{4-}$ as references.

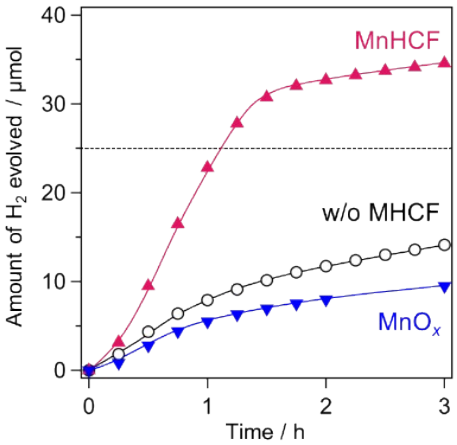

Figure S17. Time courses of H_2 evolution under visible light irradiation over MnHCF/RCO/TaON (red), MnO_x/RCO/TaON (blue), and RCOTaON (open) in the presence of 0.5 mM SiV^{IV} in aqueous KH_2PO_4 solution (50 mM KH_2PO_4, pH 4.5, 100 mL). Dotted lines show the amount of H_2 evolution corresponding to one electron donation by SiV^{IV}. MnO_x was deposited on RCO/TaON by photodeposition method. RCO/TaON (50 mg) was suspended in aqueous solution of 2.5 mM $MnCl_2 \cdot 4H_2O$ (2.5 mM, 100 mL). The suspension was irradiated with visible light ($\lambda > 400$ nm) for 2 h.

References

1 M. Weishaupt and J. Strähle, *Zeitschrift anorg allge chemie*, 1977, 429, 261–269.

2 A. M. Kusainova, S. Y. Stefanovich, V. A. Dolgikh, A. V. Mosunov, C. H. Hervoches and P. Lightfoot, *J. Mater. Chem.*, 2001, 11, 1141–1145.

3 J. J. Altenau, M. T. Pope, R. A. Prados and Hyunsoo. So, *Inorg. Chem.*, 1975, 14, 417–421.

4 O. Tomita, H. Naito, A. Nakada, M. Higashi and R. Abe, *Sustainable Energy Fuels*, 2022, 6, 664–673.

5 O. Tomita, K. Tachizawa, T. Kido, H. Suzuki, A. Nakada and R. Abe, *Adv Funct Materials*, 2025, 35, 2505908.

6 X. Lamprecht, F. Speck, P. Marzak, S. Cherevko and A. S. Bandarenka, *ACS Appl. Mater. Interfaces*, 2022, 14, 3515–3525.

7 L. Wang, Y. Lu, J. Liu, M. Xu, J. Cheng, D. Zhang and J. B. Goodenough, *Angew Chem Int Ed*, 2013, 52, 1964–1967.

8 L. Chen, H. Shao, X. Zhou, G. Liu, J. Jiang and Z. Liu, *Nat Commun*, 2016, 7, 11982.

9 D. R. Shankaran and S. S. Narayanan, *Fresenius' Journal of Analytical Chemistry*, 1999, 364, 686–689.

10 O. Makowski, J. Stroka, P. J. Kulesza, M. A. Malik and Z. Galus, *Journal of Electroanalytical Chemistry*, 2002, 532, 157–164.

11 M. Giorgetti, L. Guadagnini, D. Tonelli, M. Minicucci and G. Aquilanti, *Phys. Chem. Chem. Phys.*, 2012, 14, 5527.

12 L. Guadagnini, D. Tonelli and M. Giorgetti, *Electrochimica Acta*, 2010, 55, 5036–5039.

13 B. Wang, Y. Han, X. Wang, N. Bahlawane, H. Pan, M. Yan and Y. Jiang, *iScience*, 2018, 3, 110–133.

14 D. Ellis, M. Eckhoff and V. D. Neff, *J. Phys. Chem.*, 1981, 85, 1225–1231.

15 J. Song, L. Wang, Y. Lu, J. Liu, B. Guo, P. Xiao, J.-J. Lee, X.-Q. Yang, G. Henkelman and J. B. Goodenough, *J. Am. Chem. Soc.*, 2015, 137, 2658–2664.

16 R. Benedek, *J. Phys. Chem. C*, 2017, 121, 22049–22053.

17 J. C. Hunter, *Journal of Solid State Chemistry*, 1981, 39, 142–147.

18 H. N. Wilson and J. G. M. Bremner, *Q. Rev. Chem. Soc.*, 1948, 2, 1–24.

19 H. G. Dion and P. J. G. Mann, *The Journal of Agricultural Science*, 1946, 36, 239–245.